Elucidating the Thermal Response of W-Ta Alloys with Transient Grating Spectroscopy, TEM and Atomistic Simulation

Yildirim, E.; Jimenez-Melero, Enrique; Dacus, B.; Bennett, C.; Woller, K. B.; Short, M.; Mummery, P. M.

DOI:
10.1016/j.fusengdes.2024.114676

Document Version
Publisher's PDF, also known as Version of record

Citation for published version (Harvard):
Yildirim, E, Jimenez-Melero, E, Dacus, B, Bennett, C, Woller, KB, Short, M & Mummery, PM 2024, 'Elucidating the Thermal Response of W-Ta Alloys with Transient Grating Spectroscopy, TEM and Atomistic Simulation', *Fusion Engineering and Design*, vol. 208, 114676. https://doi.org/10.1016/j.fusengdes.2024.114676

Fusion Engineering and Design 208 (2024) 114676

Contents lists available at ScienceDirect

Fusion Engineering and Design

journal homepage: www.elsevier.com/locate/fusengdes

Elucidating the thermal response of W-Ta alloys with Transient Grating Spectroscopy, TEM and atomistic simulation

E. Yildirim [a,b,*], E. Jimenez-Melero [a,d], B. Dacus [c], C. Dennett [c], K.B. Woller [c], M. Short [c], P.M. Mummery [b]

[a] Department of Materials, The University of Manchester, Manchester, M13 9PL, Lancashire, UK
[b] School of Engineering, The University of Manchester, Manchester, M13 9PL, Lancashire, UK
[c] Department of Nuclear Science and Engineering, 77 Massachusetts Ave, Cambridge, 02139, MA, USA
[d] School of Metallurgy and Materials, University of Birmingham, Birmingham, B15 2TT, Birmingham, UK

ARTICLE INFO

MSC:
0000
1111

Keywords:
Tungsten–tantalum alloys
Irradiation
Thermal properties
Molecular dynamics
TEM

ABSTRACT

Critical for tungsten alloys' use as plasma-facing component materials are their thermal response and their evolution under irradiation. Utilising Transient Grating Spectroscopy, TEM, and Molecular Dynamics, this study sought to probe these changes in W, W6Ta, and W11Ta alloys. Irradiation with 12.25 MeV W^{6+} ions was carried out in the CLASS facility at MIT at a temperature of 500 °C for doses of 0.1, 0.3, and 1.0 dpa. The alloys' thermal diffusivity was found to degrade less than that of the pure counterpart. Molecular Dynamics simulation revealed that this was due to a reduced defect population below TEM resolution. Despite these alloys showing enhanced resilience to thermal property degradation, it was found that the absolute values of their thermal diffusivity remained below that of pure tungsten. This study highlighted a key interplay between enhancing radiation tolerance with alloying additions and the alloy additions' initial negative effect on the thermal response and thus in-service behaviour.

1. Introduction

Tungsten (W) and its alloys have been the subject of study for use in nuclear fusion devices for many decades. Specifically, W has been touted as a candidate material for the divertor region of many fusion devices. Any candidate material must contend with high heat fluxes, 14.1 MeV neutron irradiation, plasma surface interaction [1], and transmutation of elements [2], leading to a multitude of challenges to overcome [3,4]. Due to its high thermal conductivity, high melting point, high temperature strength, and low sputtering yield prior to high-dose irradiation, W emerged as the primary material for devices such as the ITER project [5]. Although these attributes have led to W being the frontrunner for this region, issues with low-temperature brittleness [6,7], formation of brittle phases under transmutation [8], irradiation-induced hardening [9], reduction of thermal conductivity [10], and recrystallisation embrittlement [11] have led to the desire to alloy W to improve these properties.

Refractory metal addition has been suggested as a route to improve W while maintaining many of its more desirable properties, such as its high melting point and strength [12]. Despite the high initial radioactivity of elements such as Molybdenum (Mo) [13] and Tantalum (Ta) [14], the latter has gained traction for use in a binary alloy system because its radioactivity is more short lived, thus meeting the 100-year target for reduced activation materials [15]. Ta has gained further attention due to its inhibition of brittle Rhenium (Re) σ-phase formation under irradiation [16], improved bending strength, crack resistance under thermal loads [17,18], resistance to blistering under plasma-surface interaction [19,20], increased recrystallisation temperature and suppression of void formation under irradiation [12,21]. There has been some evidence of increased ductility with Ta addition in computational studies, but this has not been seen in experiments. Indeed, the opposite has been observed with an increase in the already high DBTT with Ta additions [12,22]. Other potential component performance problems may arise from the reduction in thermal properties by alloying alone detailed in Nogami et al.'s recent comprehensive look into the alloy system [12]. With surface temperatures of W-based components already being >1000 °C and evidence of a reduction in thermal properties with irradiation, the thermal properties of W alloys are an important area of study.

Studies of the thermal response of pure W have found a specific influence of smaller defects. Reza et al. [23] used a mixture of molecular statics and Transient Grating Spectroscopy (TGS) to study

* Corresponding author at: Department of Materials, The University of Manchester, Manchester, M13 9PL, Lancashire, UK.
E-mail address: emre.yildirim@manchester.ac.uk (E. Yildirim).

https://doi.org/10.1016/j.fusengdes.2024.114676
Received 28 May 2024; Received in revised form 16 September 2024; Accepted 17 September 2024

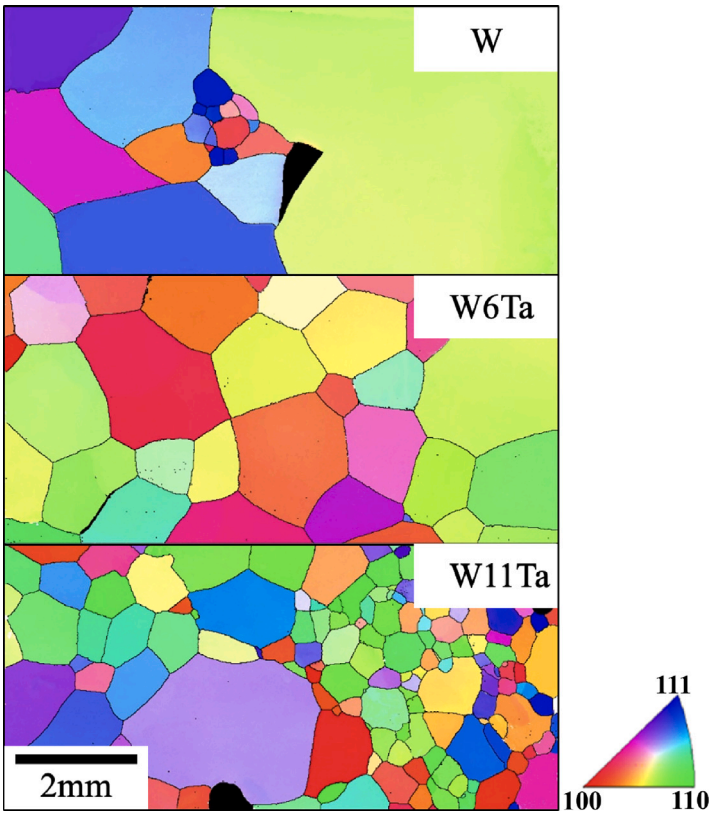

Fig. 1. Figure detailing exemplar EBSD maps generated for each sample composition. The beam energy was 20 kV and a 50 μm step size. The black areas mark pores formed during the arc melting process.

the different contributions of dislocation loops and small vacancy defects after irradiation. They concluded that the vacancies remaining after recombination played an important role in the drop in the measured thermal diffusivity. Similar conclusions have also been drawn elsewhere. Ferry et al. [24], when studying the thermal response of Si-irradiated single crystal Niobium (Nb), found an initial drop and then a subsequent recovery of the thermal diffusivity, consistent with TEM observations. With this correlation in mind, Ta addition and the effect on defect populations could show commensurate changes to the thermal response. To study the effect of Ta addition, molecular dynamics work by Qiu et al. [25] showed little difference in defect populations during damage cascade simulations of different alloy compositions, while the proton irradiation work by Ipatova et al. [26] and the self-ion irradiation work by Yi et al. [27] have shown a larger density and smaller size of dislocations. Therefore, it is of interest to investigate the influence of small defects on thermal properties. To study the effect of irradiation on the thermal properties of W-Ta alloys, this study utilises Transient Grating Spectroscopy (TGS) to measure the thermal response, and Transmission Electron Microscopy (TEM) and Molecular Dynamics (MD) to investigate defect production and evolution.

2. Methods

2.1. Materials

The alloys for this study were made at the University of Sheffield through the Royce Access Scheme by arc melting a W rod (diameter 5 mm, Alfa Aesar, ≤ 30 appm impurity elements) with Ta wire (diameter 2 mm, Alfa Aesar, ≤ 30 appm impurity elements) in a copper crucible under high vacuum and back-filled with Argon (Ar). Each button was flipped 15 times to allow homogenisation during melting. The composition of each material produced was pure W, W-6wt% Ta, and W-11wt% Ta (labelled W, W6Ta and W11Ta throughout) with no other elements beyond trace quantities measured by X-ray fluorescence (XRF) (all other elements were found to be < 0.05wt%, the full verification can be found in the data repository of this article). The samples were then cut by Electrical Discharge Machining (EDM) to form samples of dimensions 5 × 10 × 2 mm^3, one for each irradiation condition, and polished up to a 40 nm colloidal silica mirror finish after grinding with SiC paper from p800-p4000 grits. Example EBSD (Electron BackScatter Diffraction) maps are shown in Fig. 1. The average grain sizes of each composition are: 2090 ± 1702 μm, 947 ± 238 μm and 749 ± 101 μm.

2.2. W-ion irradiations

Irradiations were carried out at the CLASS Facility at the Massachusetts Institute of Technology (MIT) at temperatures of ≈ 500 °C (497 ± 20.6 °C across all exposures, heat rate of 5 °C/min) and an average flux of 1.96×10^{15} $ionsm^{-2}s^{-1}$ with the experimental arrangement shown schematically in Fig. 2. The temperature was monitored using a 2-colour IR pyrometer and the beam current was measured using a Faraday cup. 12.25 MeV W^{6+} W ions were used, with the penetration depth calculated via SRIM (Stopping Range for Ions in Matter) [28] (Fig. 3). The SRIM calculation was performed with the Quick Kinchin–Pease method with the binding energy set to 0eV using the method from Stoller et al. [29] and W displacement threshold of 90 eV as per [30]. Damage levels of 0.1, 0.3 and 1.0 dpa were used to allow insight into the behaviour of the thermal property in a DEMO reactor (the final dose is ~0.1 dpa for the first ITER divertor [31] and dose rates of ~3 dpa/fpy (displacements per atom per full power year) in the DEMO divertor and up to 9 dpa/fpy at the first wall for plasma-facing W components [32,33]).

2.3. Transient Grating Spectroscopy (TGS)

In order to probe the thermal response of the very shallow damaged layer, TGS was used to reduce the influence of the bulk material on the

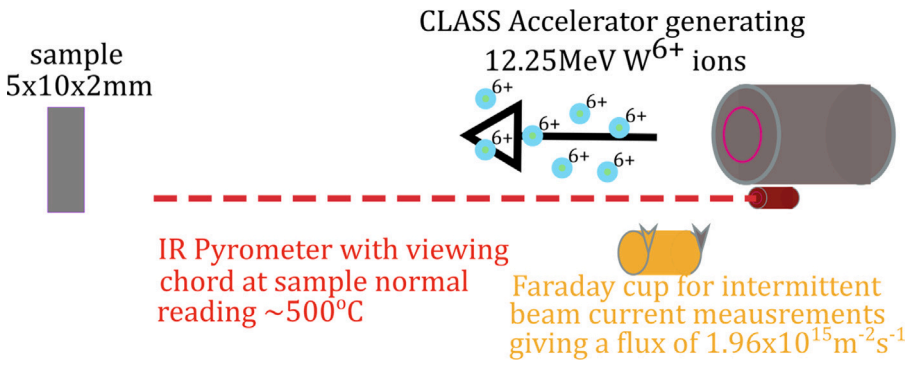

Fig. 2. Schematic of the experiment set-up at the CLASS facility, detailing the temperature, flux and diagnostics.

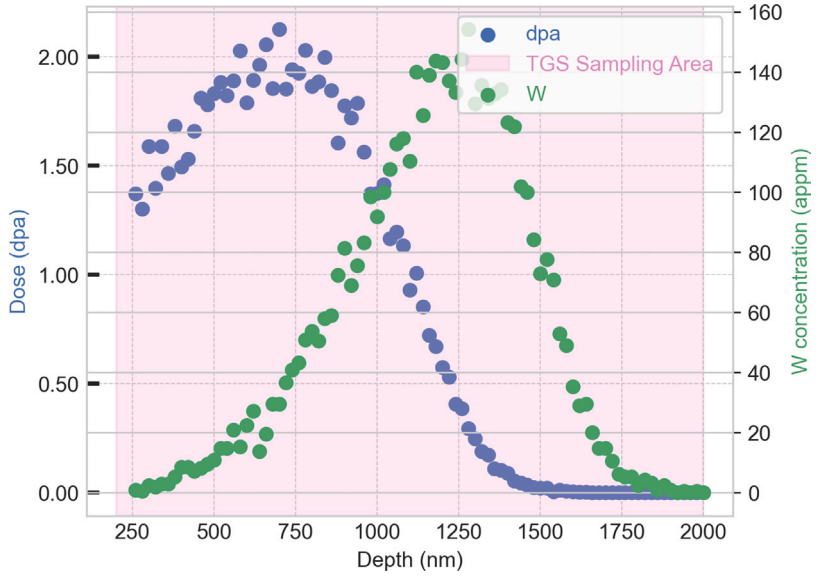

Fig. 3. Figure showing the damage depth distribution in addition to the probe depth of the TGS. Note that due to the probe depth all thermal diffusivity measurements of irradiated materials will have contributions from the bulk, but as the relative change is being studied, this effect is constant across each composition and condition.

measured diffusivity values. Two 532 nm probe lasers formed a grating spacing of $\lambda_{grat} = 6.4$ μm giving an approximate probe depth of ≈ 2 μm (estimated as λ_{grat}/π [34]) with a sampling rate of 1 kHz. This is shown in Fig. 3 superimposed on the damage profile. TGS was used to measure the thermal diffusivity of the material at each damage state in an *ex-situ* setup at room temperature. For further details on the technique, see the works by Hofmann et al. [35,36], Dennett et al. [37] and Wylie et al. [38].

2.4. Transmission Electron Microscopy (TEM)

TEM was performed on a FEI Talos F200 system on samples made on a FEI Helios 660 Gallium (Ga) Focused Ion Beam (FIB). FIB liftouts were performed at 30 kV from random areas within the damaged region with sample sizes of 10x20x1 μm. These were attached to a molybdenum grid and initially thinned down to ≈ 170 nm with an 80 pA 30 kV Ga beam, with an expected damage depth of ≈ 20 nm. They were further thinned using a 39 pA 2 kV Ga beam with an expected damage depth of ≈2 nm. The damage depths were calculated as described in Section 2.1 for a Ga incident ion. While this damage depth is small and any generated defects from the FIB were expected to escape to the surface, FIB damage is seen in Fig. 6. An example of a lift-out and the analysed region can be found in the supplementary information. STEM images were taken with the (200) reflection excited, consistent with viewing loops with expected Burgers vectors of either [100] or [111]. These images were used at a consistent magnification for semi-automated analysis of the dislocations, with 3 micrographs per sample being used. The sample thickness was measured with CBED (Convergent Beam Electron Diffraction) for each composition and was averaged for three different points per lamellae as per [39] (also shown in the supplementary information). The lamellae thickness ranged from 90–140 nm across all the samples. All measurements of foil thickness in the sample had a variation of less than 10%. A cut-off diameter of 5 nm was chosen based on the maximum size of the FIB defects in this work. Due to the irregular and varied shape of the dislocations, the dislocation area was recorded and converted to an equivalent diameter (approximated as a perfect circle of area πr^2).

2.5. Molecular Dynamics (MD)

MD simulations were employed to further study defect generation behaviour and population. Although the timescales and the size of the simulations were not enough to capture statistically useful loop formation, they are used here to give insight into initial defect populations and agglomeration. Using the EAM / FS potential of Chen et al. [40], a PKA (Primary Knock-on Atom) damage cascade simulation was ran using 432,000 atoms in a simulation box of 60a × 60a × 60a (a being the lattice parameter of 3.165 Å) and a PKA input at a random location with an energy of 10 keV. A total of 20 PKAs were simulated with a distance-limited variable timestep. This limited the maximum distance that a particle can move in each timestep to control the highly energetic particles at the beginning of the cascade.

After equilibrating the system at 500 °C for 1.25 ps, a PKA was created by deleting a random atom and creating an atom in its place with an energy of 10 keV. The timestep of each PKA cascade was limited between 10^{-8} *ps* and 10^{-3} *ps* for a series of four distance-limited timestep runs. The first 150,000 timesteps were distance limited to 0.00025 Å, then the next 150,000 to 0.001 Å, subsequent 75,000 to 0.005 Å, and the final 25,000 time steps to 0.01 Å . After these timesteps were completed, a subsequent PKA was generated and the process was repeated up to a total of 20PKAs. Periodic boundary conditions were used and atoms were held at a temperature of 500 °C to match the irradiations with the simulations run in an NVE micro-canonical fashion. Each simulation was performed on LAMMPS version 29-Sep-2021 on 48 cores. Visualisation was performed with OVITO software [41] and defect identification was conducted using OVITO's Wigner–Seitz function, with cluster analysis performed using a cutoff distance of 1.1a. The files to run these simulations can be found in the GitHub repository linked to this paper.

3. Results

3.1. Thermal diffusivity

The thermal diffusivity results are presented in Table 1 and are shown graphically in Fig. 4. These detail changes in both the measured absolute and normalised values of the thermal diffusivity with irradiation damage, with additional data from the literature [12,42]. The absolute values show an initial drop in thermal diffusivity with alloying content, consistent with the existing literature on changes in thermal properties of irradiated materials, including pure W [38, 42,43]. The change between 0.1 and 0.3 dpa for the W11Ta system showed an significant increase while all other compositions and doses show a slight change in thermal diffusivity with irradiation between 0.1 dpa and 1.0 dpa, but no increase with a high degree of statistical significance. All these changes less than 2% and within the error bars of other measurements. The final absolute values at 1 dpa showed a decrease of 29.5%, 25.7% and 22.0% for W, W6Ta, W11Ta respectively. Normalised data in Fig. 4 show the same saturation in diffusivity but with the greatest reduction in the unalloyed material, suggesting a greater effect of irradiation damage. The values of thermal diffusivity appear to have saturated for sample W and W6Ta at 0.1 dpa. For W11Ta, this seems to occur at 0.3 dpa with the difference between 0.1 dpa and 0.3 dpa values showing a point-by-point change greater than 2%. This suggests a delay in the saturation for this alloy.

The differences in diffusivity between the compositions are large in the virgin state and remain large after irradiation. The initial difference from unalloyed W is 41.5% for W-W6Ta and 50.7% for W-W11Ta with the final difference being 38.4% and 45.4% for W-W6Ta and W-W11Ta respectively.

3.2. Microstructural analysis

An overview of the microstructures is shown in Fig. 5 with high-magnification images shown in Fig. 6. The defect diameter distributions are given in Fig. 8 and the defect number density changes in Fig. 9. All compositions show contributions of both dislocation loops and loop chains at all damage levels, which can be seen further in Fig. 7. This shows a series of loops in a chain with dislocation lines also seen, in addition to singular loops. Higher magnification images further show this and show the relatively little change in dislocation morphology with increasing dose as can be seen by comparing images of 0.1 dpa and 1 dpa samples in Fig. 6. Fig. 6 shows the damage induced by the FIB preparation method. This damage will be present in the micrographs of the irradiated material, but it is clearly smaller in size and can be identified and removed from the quantitative analysis.

The loop number density for the alloy compositions is higher at all irradiated levels, with the average for the W11Ta is higher than the

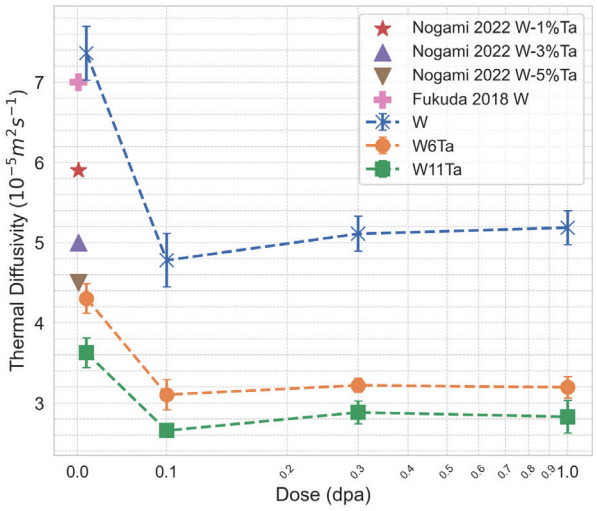

(a)

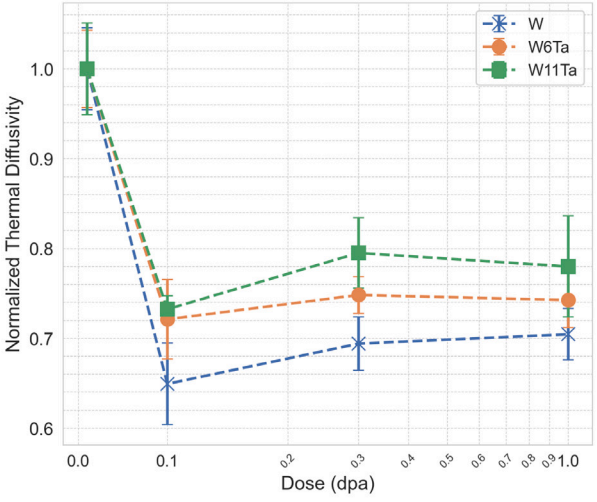

(b)

Fig. 4. (a) Graphs detailing the thermal diffusivity changes with irradiation, in addition to W-Ta samples from elsewhere measured through the laser flash method [12,42] and (b) details the normalised thermal diffusivity change to allow for further visualisation of the percentage changes across each sample. The error bars were calculated based on both the experimental distribution and the uncertainty in the measurements, with these being one-sigma errors. The pristine values are slightly offset from 0 dpa for clarity with the additional data.

Table 1
Overview of the irradiation conditions and final values for the thermal diffusivity at different damage levels.

Sample	Damage (dpa)	Temperature (°C)	Flux ($m^{-2}s^{-1}$)	Thermal diffusivity (10^{-5} m^2s^{-1})
W	0	–	–	7.36 ± 0.34
	0.1	515.0 ± 33.2	1.96×10^{15}	4.78 ± 0.33
	0.3	491.0 ± 14.3	1.96×10^{15}	5.11 ± 0.22
	1	487.5 ± 18.0	1.96×10^{15}	5.19 ± 0.21
W6Ta	0	–	–	4.30 ± 0.19
	0.1	510.2 ± 25.1	1.96×10^{15}	3.10 ± 0.19
	0.3	499.0 ± 22.8	1.96×10^{15}	3.22 ± 0.09
	1	482.1 ± 17.3	1.96×10^{15}	3.19 ± 0.13
W11Ta	0	–	–	3.62 ± 0.18
	0.1	488.5 ± 28.7	1.96×10^{15}	2.65 ± 0.05
	0.3	512.4 ± 19.1	1.96×10^{15}	2.88 ± 0.14
	1	505.2 ± 19.6	1.96×10^{15}	2.83 ± 0.20

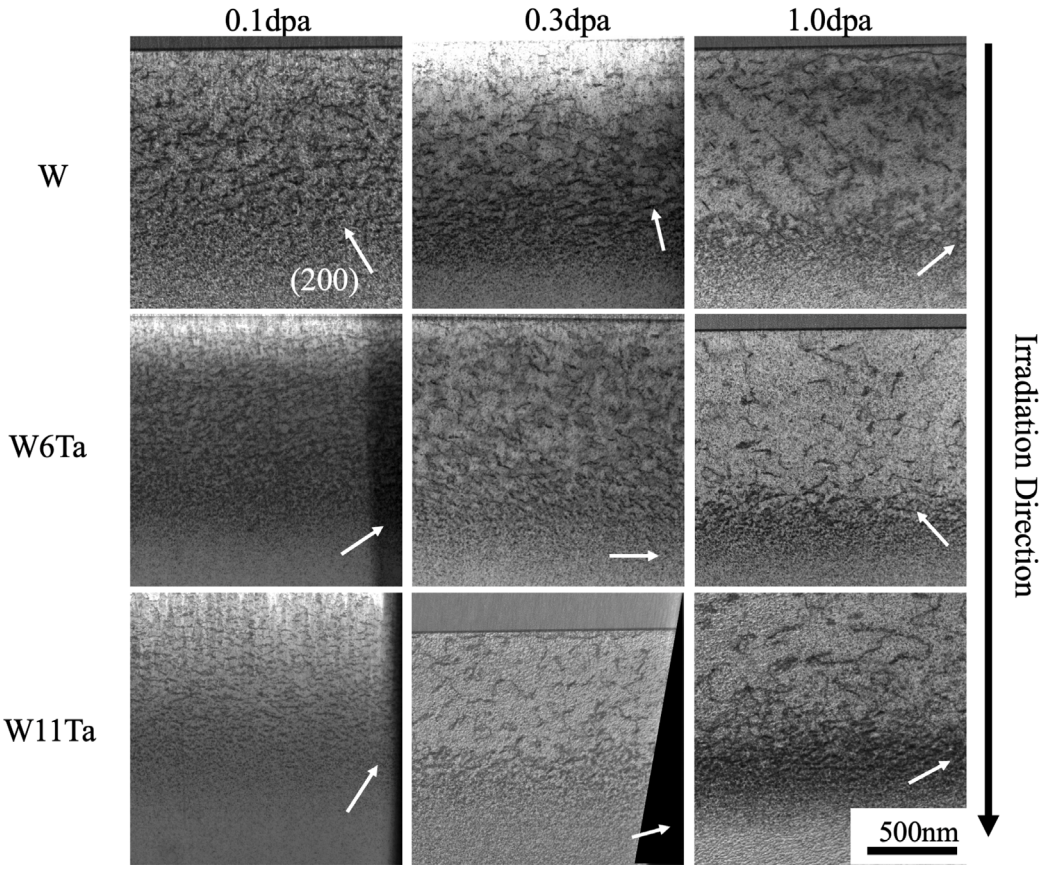

Fig. 5. An overview of the microstructures through Bright Field STEM images, with the (200) reflection highlighted with a white arrow in each micrograph.

Table 2
Data for final microstructures at each dpa, in addition to the MD simulations for the final defect population after 20 PKAs generated in the system. In addition, the fraction of either interstitials or vacancies in a cluster (within 1.1a of another defect of the same type) is also listed.

Sample	TEM			MD		
	Damage (dpa)	Loop number density ($\times 10^{21}$ m^{-3})	Loop size (nm)	Final defect population	Interstitial cluster fraction	Vacancy cluster fraction
W	0.1	7.34 ± 1.83	10.58 ± 5.90	259 ± 29	0.37	0.12
	0.3	7.24 ± 0.93	11.03 ± 7.08			
	1	8.21 ± 0.97	12.13 ± 8.57			
W6Ta	0.1	12.74 ± 1.65	11.25 ± 6.84	234 ± 11	0.27	0.11
	0.3	9.95 ± 2.17	10.63 ± 1.52			
	1	10.63 ± 1.52	11.14 ± 7.65			
W11Ta	0.1	16.84 ± 2.93	9.79 ± 4.57	223 ± 20	0.29	0.08
	0.3	15.95 ± 3.17	8.11 ± 6.31			
	1	12.80 ± 2.61	10.70 ± 6.58			

W6Ta in all damage levels. The evolution of the number density for the alloys follows a weak negative trend with increasing dose, while pure W shows a slight increase in the number density with each damage level. The trends in diameter changes are less clear, but there is an increase in the largest dislocations at the highest dpa with a positive trend for the pure sample and the W11Ta, but these trends are weak (see Table 2).

3.3. Atomistic simulation

Snapshots of the molecular dynamics simulations at 1, 10 and 20 PKAs are seen in Fig. 10. The values for the evolution of the defect number per PKA and the final interstitial and vacancy cluster fractions are shown in Figs. 11 and 12. Due to the short timescale, with interest being the generation of Frenkel pair populations, it is only the clustering (interstitials of vacancies closer than 1.1 *a*) and not extended defects such as dislocations are simulated. These show a reduction in the number of defects with Ta addition. The evolution of these defects shows an increase in the number of defects with increasing PKA cascades. For all compositions, an initially steep gradient showed rapidly increasing defect numbers at low PKA numbers, with this rate of damage accumulation slowing with more PKAs cascades. The effect of Ta showed a decrease in the number of defects accumulated at each PKA, which became more pronounced at higher PKAs. With increasing Ta addition, the number of defects reduced, but the change between W and W6Ta was much less than the difference between W6Ta and W11Ta.

For all alloys, there is significantly greater interstitial agglomeration than vacancy agglomeration. The W6Ta showed the least interstitial agglomeration and the W11Ta showed the smallest vacancy cluster fraction, with both showing reduced clustering compared to pure W. This suggested some inhibition of defect agglomeration when alloying.

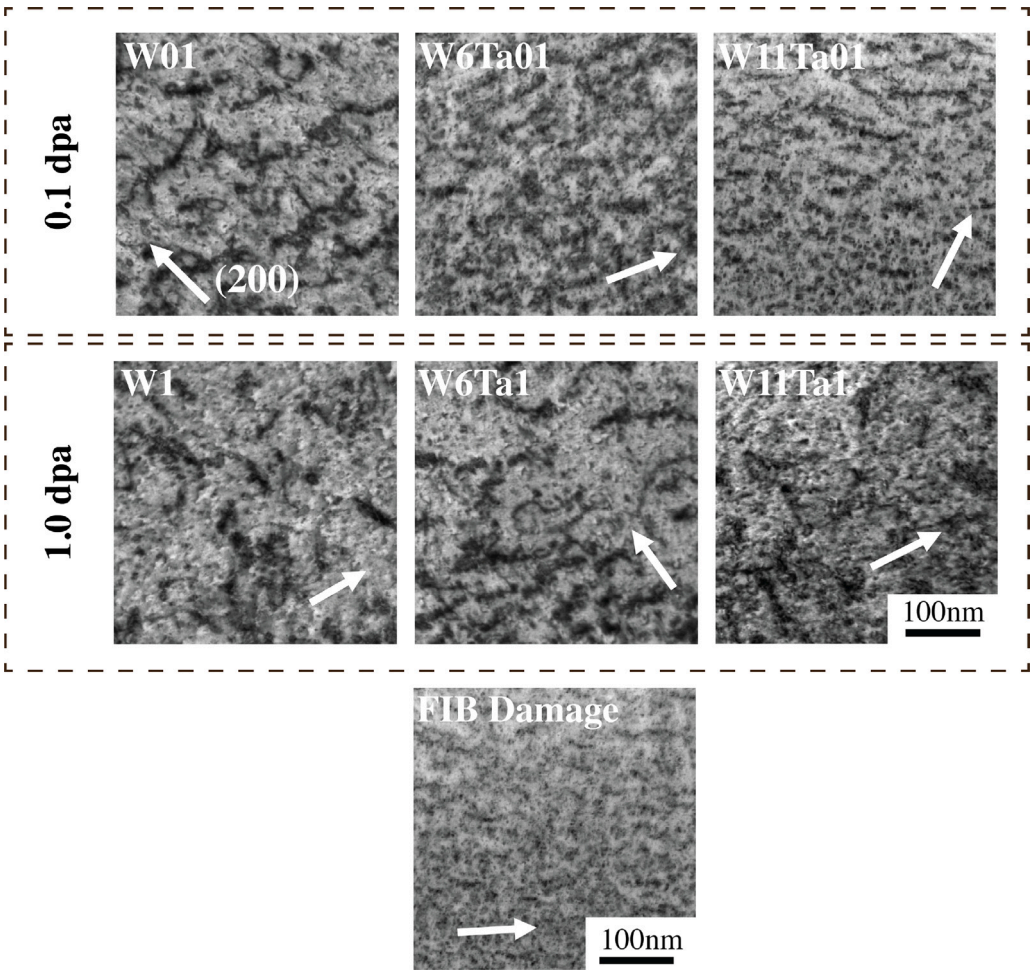

Fig. 6. Higher magnification STEM micrographs of loops and loop chains within each composition at both 0.1 and 1.0 dpa. Additionally an image of the damage created by the FIB preparation is also seen. Again the (200) reflections are highlighted with a white arrow in each image, indicating the plane normal.

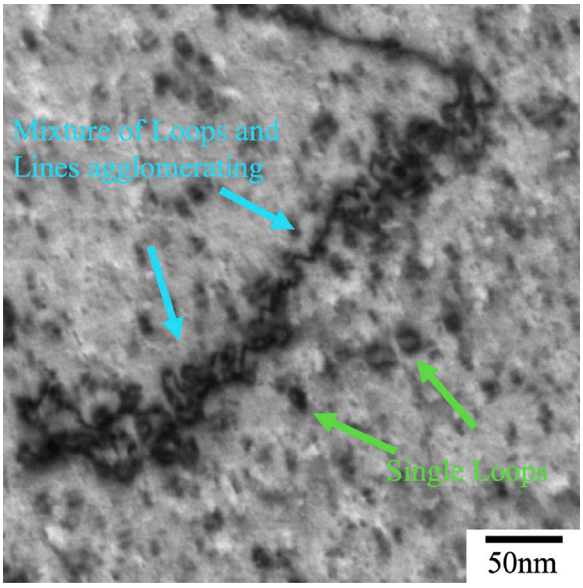

Fig. 7. STEM image of sample W01 (a dose of 0.1 dpa) highlighting both the loops chain, an amalgamation of loops and lines, and of singular dislocation loops that formed under irradiation.

4. Discussion

4.1. Unirradiated thermal diffusivity values

Quantitative comparisons can be made for the unirradiated values. The work presented here (Fig. 4) is consistent with the work of other studies such as Nogami et al. [12] and Fukuda et al. [42]. Alloying decreases the thermal properties through straining of the lattice providing scattering centres for electron and phonon thermal transport in the sample. Ta in solid solution provides small strains in the lattice, affecting phonon transport, while electronic contributions from the Ta also reduce the thermal diffusivity. The thermal diffusivity of Ta itself sits far below that of W, at 2.42×10^{-5} m^2s^{-1} [44] compared to W's measured diffusivity of $\approx 7 \times 10^{-5}$ m^2s^{-1}. This implies a contribution from the innately lower thermal diffusivity of the Ta atoms and the contribution through the lattice strains caused by solid solution. It is clear that alloying has a significant effect on thermal properties. To compare with the effects of irradiation, alloying with 6% Ta gave a greater reduction than irradiating unalloyed W in this study and pure W irradiated at room temperature and annealed at 400 °C in Reza et al. [45]. Alloying with W11Ta in this study is comparable to a similar decrease as irradiating pure W at RT and annealing at 200 °C [38] and with proton irradiations by Habainy et al. [46] up to damage levels of 5.8 dpa. Alloying effects have been shown to be less pronounced at higher temperatures [42], but such a significant drop is likely still to play a part during operation. This has a twofold effect in that the design of new alloy systems must account for these changes, and that

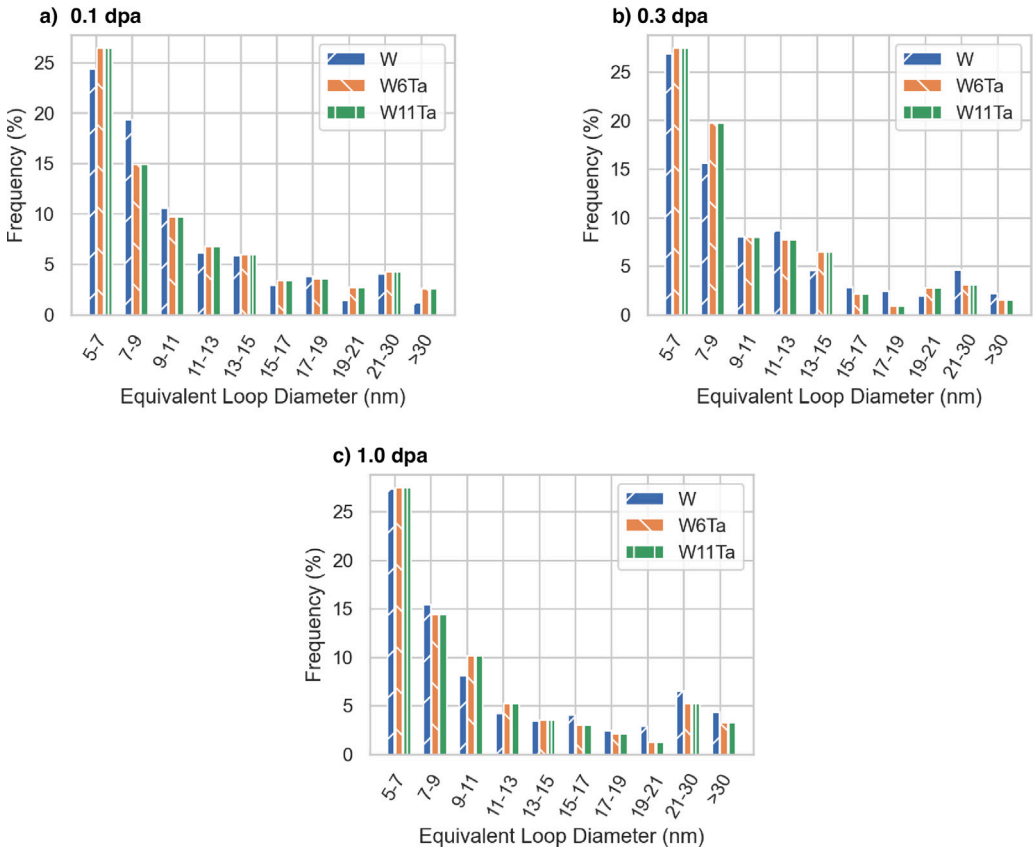

Fig. 8. Histograms of the dislocation loop equivalent diameter distribution for each damage level of (a) 0.1, (b) 0.3 and (c) 1.0 dpa as taken from the TEM micrographs.

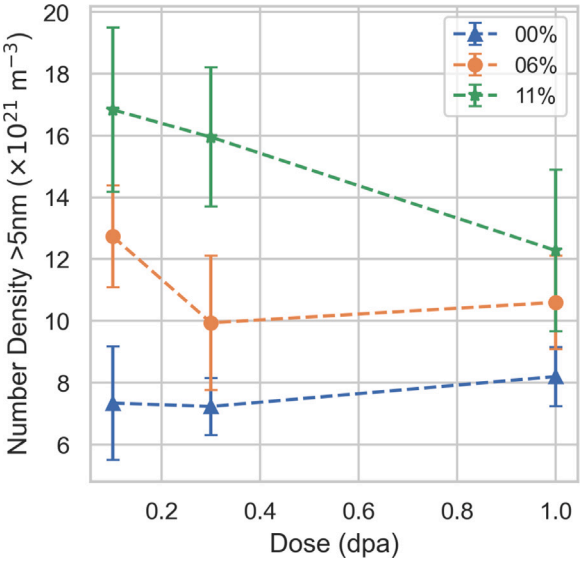

Fig. 9. Loop number density evolution with damage across each composition as measured in the TEM micrographs, showing consistently higher dislocation densities across the alloyed samples. The Ta content in each same is highlighted by a different colour, indicated in the legend.

in systems where the thermal properties are a priority, alloying may not always be useful depending on the total dose of the component. The increases in temperature caused by this reduced thermal transfer could lead to different recovery kinetics under irradiation (W has been shown to recover defects at temperatures similar to operating temperatures [1,47], and fully recover at temperatures ≈ 300 °C above it [48]) and affect the diffusion processes of plasma species and transmutation products. Therefore, this means that a comparison between irradiations at the same temperatures for different alloy systems may not be representative of the reactor environment if these alloy systems replace, e.g., W in the divertor. This would be due to the temperature of an alloyed component being higher than that of a pure W component, meaning the potential for different damage morphologies. Indications of these effects have been seen in [49] where Ta addition, known to be beneficial for reducing the extent of surface modification in W by plasma species [20,50], performed more poorly under ELM-like conditions, suggested to be due to the reduced thermal conductivity still having an effect at elevated temperature, causing a great increase in surface temperature, thus surface modification.

4.2. Alloying effects on defect structures

The dislocation structures presented here demonstrate an increase in the loop number density with alloying composition (Fig. 9). This is consistent with the work of Yi et al. at the same temperature for pure W and a 5%Ta alloy. Overall, the alloyed samples also showed an increase in smaller dislocations across all damage levels. The number of defects under 10 nm was consistently higher in all alloy compositions. This would imply a reduction in the ease of formation of loop chains with alloying and therefore smaller dislocation diameters were recorded. This can be associated with an increase in the Peierls stress by alloying and is consistent with the experimental works by Yi et al. [27] and Ipatova et al. [26] which demonstrated an increased number density and reduced size of defects with Ta alloys, and with computational studies [25,51] predicting an increase in Peierls stress. The cut-off diameter for quantitative analysis for the dislocation was used as 5 nm. across each sample. This was required to not include FIB damage, but defects in Ta alloyed samples have been seen to be below 5 nm

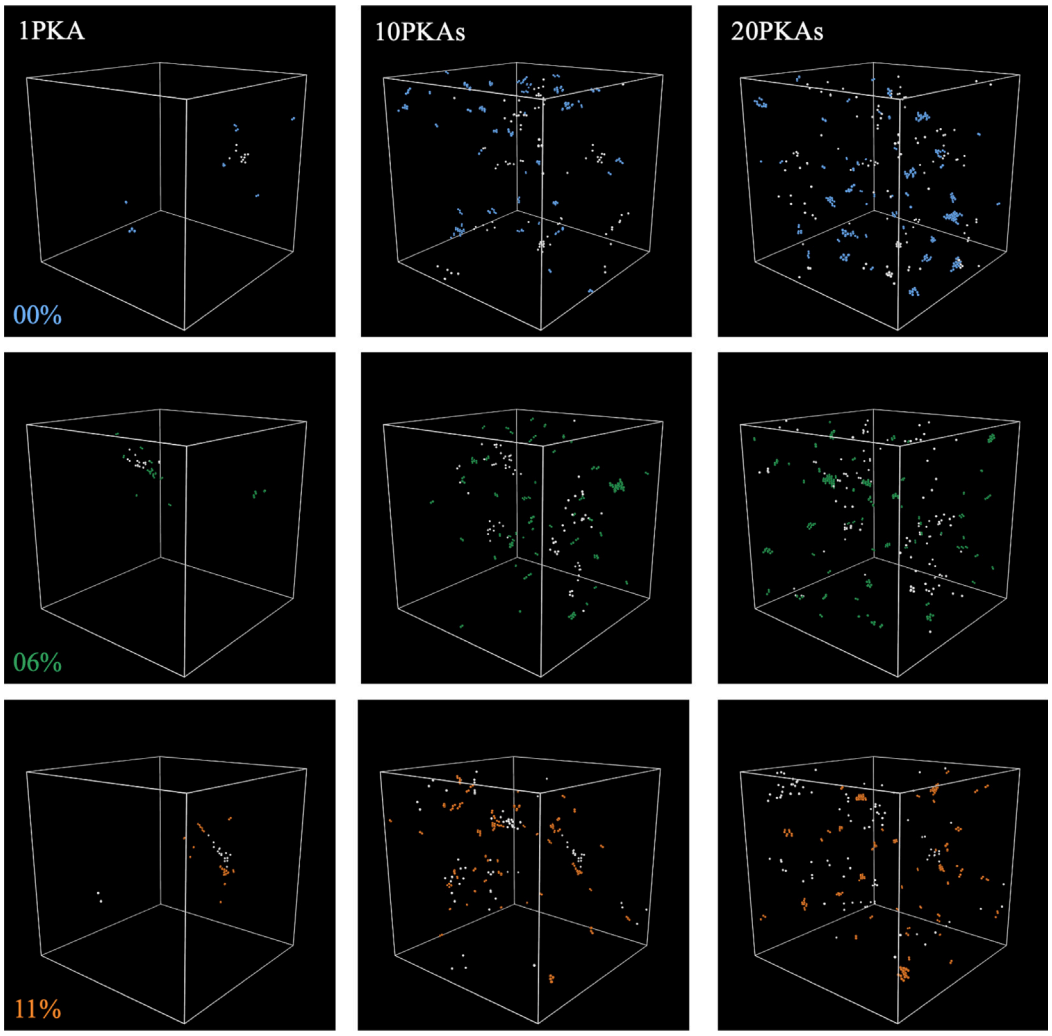

Fig. 10. Snapshots of the cascade evolution at PKA numbers of 1, 10 and 20PKAs. The white dots represent vacancies across each image, and the atoms with colour represent interstitials.

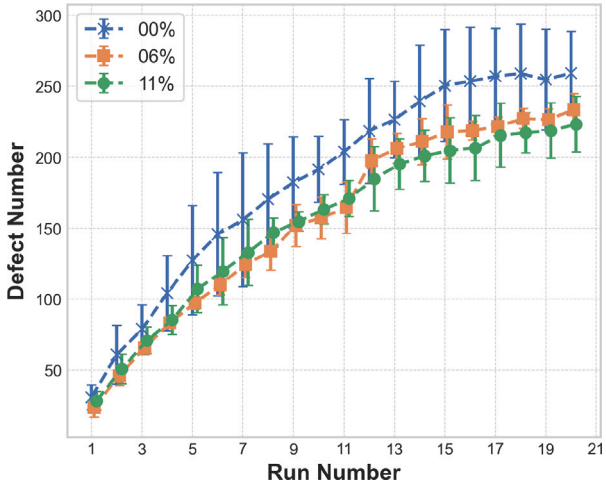

Fig. 11. Figure showing the number of defect present in the simulation box evolving with increasing PKA number. The alloyed samples showed a reduction in final Frenkel pairs produced when compared to the pure W.

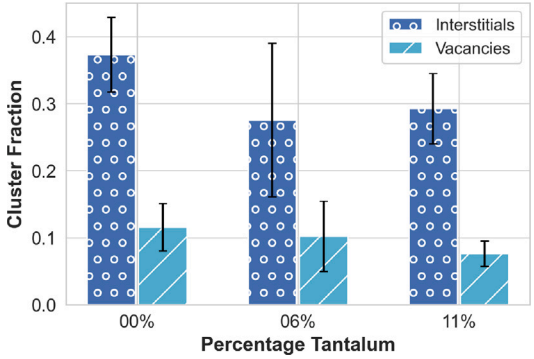

Fig. 12. Fractions of interstitial and vacancies clusters within each alloy composition demonstrating a weak trend in clustering reduction with alloy addition.

elsewhere [26] and therefore may have been present in these sample too. Other works such as Yi et al. [27] have found such a correlation with increased alloying, showing a reduction in loop size and an increase in density with alloying with both Ta and Re in binary systems.

The alloy samples showed a decreasing trend in the defect population with dose and a small increase in the defect size. This implied loop agglomeration with increasing dose. As the pure W values were

consistent, it implied that minimal agglomeration of loops was occurring, and rather loop growth. This may be due to the increased Peierls stress retarding the formation of loop chains in the alloy samples.

The molecular dynamics simulation showed an increase in defect recombination with the addition of Ta. This enhanced recombination led to smaller final defect number, with this effect becoming less pronounced with increasing Ta addition. Defect saturation begins to occur at high PKA numbers, where the generated Frenkel pairs are likely to interacted with defects already in the lattice to recombine. This is consistent with work on binary systems elsewhere by Jin et al. [52] that showed enhanced recombination in Ni-Fe alloy systems over much longer cascades. Some room temperature MD cascade studies in W-Ta alloys of single cascades at a range of energies did not find such recombination enhancement [25], but *ab-intio* works [53] have demonstrated a strong repulsive force of SIAs along the ⟨111⟩ crowdion direction with some weak attraction when Ta occupies the perpendicular neighbouring site to this direction and small vacancy attraction (with the study concluding this attraction to be insignificant). Overall, this would lead to enhanced defect recombination in WTa systems as seen in this study. This is consistent with alloying with Re where Positron Annihilation Spectroscopy (PAS) demonstrated a reduced number of small vacancy defects [54]. Additionally, as is shown here, such differences in defect populations can occur after multiple cascades which was not simulated by Jin. Agglomeration of these defects into clusters was observed, and the interstitials showed a greater affinity for cluster formation than vacancies. This is consistent with the mobility of interstitial-type defects compared to vacancy defects at this temperature in W [47]. This agglomeration was reduced with Ta addition, suggesting a reduced mobility of these small defects in the matrix. The demonstrates a disagreement between the experimental works showing increased number density of resolvable defects, and with the atomistic simulations showing a reduced number of Frenkel pairs. The implication is that the resolvable defects populations have a different trend to those simulated during the PKA cascades. Defect populations have a critical effect on the thermal properties, and thus measurement of the thermal properties can further elucidate the defect populations. Therefore, irradiated thermal properties are critical for understanding the evolution of the defect.

4.3. Irradiated thermal diffusivity

The measured absolute value will have contributions from the undamaged bulk due to the probe depth of the TGS profile. Hence, care should be taken when making a quantitative comparison with other studies. At the lowest damage level of 0.1 dpa all compositions show the greatest reduction in thermal diffusivity. Point-by-point changes beyond 0.1 dpa are minimal for all alloys, apart from in between W11Ta01 and W11Ta03, suggesting that a level of saturation has occurred within pure and W6Ta at 0.1 dpa and 0.3 dpa in the W11Ta system. Saturation by 0.1 dpa is consistent with work in pure W elsewhere by Wylie et al. [38] but seen at a higher dose of 1 dpa in Reza et al. [23], both for room temperature irradiations. Saturation at lower damage levels in this study could be due to higher defect mobility at the higher temperatures, meaning defects would agglomerate more quickly for the same dose rate. The saturation in the W11Ta sample occurred at a higher damage level of 0.3 dpa. The profile of the W11Ta shows an initial 'drop and recovery' consistent with work in W by Wylie et al. [38] and in Nb by Ferry et al. [24]. These studies suggest this is due to ordering of smaller dislocations into larger ones. For this to be the case here, changes in the size and density of dislocations should follow the same trend as the diffusivity profile. This is not the case, implying that a different factor must be contributing to these changes, such as smaller defects than were resolvable in the TEM.

Small defects, below that of TEM resolution, have been proposed as the dominant defects on thermal property changes. This theory can be the basis for understanding the shape of the diffusivity profiles in this work. This was thoroughly investigated by Reza et al. [23] using a mixture of irradiation and molecular statics calculations. Through this, Reza demonstrated the significant influence of Frenkel pair generation and small monovacancies on the thermal diffusivity drop over that of larger defect structures. While there is an increase in the number density of TEM resolvable defect structures under irradiation with increasing Ta addition in this study and in other [27], MD has shown a reduction in Frenkel pairs produced through enhanced recombination. The atomistic simulations are consistent with the thermal diffusivity change, while the TEM resolvable defect structure trends are not. This suggests a reduction in defect population of the alloyed sample leading to an improved response to irradiation of the thermal diffusivity (demonstrated in the normalised values in Fig. 4). It follows that the reduction in Frenkel pairs produced, shown by the MD simulations, is therefore contributing to a more irradiation tolerant thermal diffusivity in the alloyed samples. This shows that these small defects play a critical role in the thermal diffusivity drop and that enhanced recombination in alloyed samples can act to reduce this drop in thermal conductivity under irradiation. This is an example of how these alloys are more tolerant to irradiation than the pure counterpart. To extend this work to broader alloy design, enhanced recombination has been demonstrated to reduce the relative change in thermal properties by enhancing the recombination of point defects. It poses the idea that some alloy additions, should they employ similar recombination behaviour, could be more beneficial than their pure or lower alloy counterparts on longer timescales. Through enhanced recombination, end-of-life values have the potential to show improvement not only on a relative basis but also on an absolute basis in some systems.

5. Conclusion and further work

Overall, this study demonstrated a significant reduction in the thermal diffusivity under irradiation of W and W-Ta alloys. The irradiation-induced reduction in thermal properties was mitigated by Ta addition, which has been suggested to be due to a reduction in defect generation and enhanced recombination in these alloy systems. While this is beneficial in terms of acting to reduce the defect production under irradiation, critically, the loss from the initial alloying stage is too great for any reduction in damage to be beneficial for these alloyed samples in terms of their thermal properties. For design of fusion components, this highlights the importance in accounting for changes in thermal properties with alloying and their behaviour under irradiation; when seeking improvement in other properties from alloying.

Further study should investigate these effects at more temperature ranges, where different defects will form under irradiation and therefore interact with the alloying elements differently. In addition, studies using techniques like PAS for the defect population could further aid in understanding the concentrations of small, below the resolution of TEM, defects and their effect on the thermal properties.

CRediT authorship contribution statement

E. Yildirim: Writing – original draft, Methodology, Investigation, Formal analysis, Data curation, Conceptualization. **E. Jimenez-Melero:** Writing – review & editing, Supervision, Methodology. **B. Dacus:** Methodology, Formal analysis, Data curation. **C. Dennett:** Methodology. **K.B. Woller:** Methodology, Investigation, Data curation. **M. Short:** Writing – review & editing, Methodology, Investigation. **P.M. Mummery:** Writing – review & editing, Supervision, Methodology.

Declaration of competing interest

The authors declare that they have no known competing financial interests or personal relationships that could have appeared to influence the work reported in this paper.

Data availability

Data will be made available on request.

Acknowledgements

We wish to acknowledge the EPSRC, UK support through grant number EP/L01663X/1, and the Henry Royce Institute through the Royce PhD Equipment Access Scheme for EY, UK to access the Arc Melting facilities at Royce @Sheffield.

Appendix A. Supplementary data

Supplementary material related to this article can be found online at https://doi.org/10.1016/j.fusengdes.2024.114676.

References

[1] R.A. Pitts, X. Bonnin, F. Escourbiac, H. Frerichs, J.P. Gunn, T. Hirai, A.S. Kukushkin, E. Kaveeva, M.A. Miller, D. Moulton, V. Rozhansky, I. Senichenkov, E. Sytova, O. Schmitz, P.C. Stangeby, G. De Temmerman, I. Veselova, S. Wiesen, Physics basis for the first ITER tungsten divertor, Nucl. Mater. Energy 20 (2019) 100696, http://dx.doi.org/10.1016/j.nme.2019.100696.

[2] X. Hu, Recent progress in experimental investigation of neutron irradiation response of tungsten, J. Nucl. Mater. 568 (2022) http://dx.doi.org/10.1016/j.jnucmat.2022.153856.

[3] M. Rieth, D. Armstrong, B. Dafferner, S. Heger, A. Hoffmann, M.D. Hoffmann, U. Jäntsch, C. Kübel, E. Materna-Morris, J. Reiser, M. Rohde, T. Scherer, V. Widak, H. Zimmermann, Tungsten as a structural divertor material, in: 5th Forum on New Materials Part B, Vol. 73, Trans Tech Publications Ltd, 2010, pp. 11–21, http://dx.doi.org/10.4028/www.scientific.net/ast.73.11.

[4] T. Hirai, S. Panayotis, V. Barabash, C. Amzallag, F. Escourbiac, A. Durocher, M. Merola, J. Linke, T. Loewenhoff, G. Pintsuk, M. Wirtz, I. Uytdenhouwen, Use of tungsten material for the ITER divertor, Nucl. Mater. Energy 9 (2016) 616–622, http://dx.doi.org/10.1016/j.nme.2016.07.003.

[5] M. Akiyoshi, L.M. Garrison, J.W. Geringer, H. Wang, A. Hasegawa, S. Nogami, Y. Katoh, Thermal diffusivity of irradiated tungsten and tungsten-rhenium alloys, J. Nucl. Mater. 543 (2021) http://dx.doi.org/10.1016/j.jnucmat.2020.152594.

[6] C. Younger, G. Wrights, Effect of Reactor Irradiation on Ductile-brittle Transition and Stress-strain Behaviour of Tungsten, Tech. Rep., NASA, Washington D.C., 1970, URL https://ntrs.nasa.gov/archive/nasa/casi.ntrs.nasa.gov/19700029060.pdf.

[7] C. Yin, D. Terentyev, T. Zhang, S. Nogami, S. Antusch, C.C. Chang, R.H. Petrov, T. Pardoen, Ductile to brittle transition temperature of advanced tungsten alloys for nuclear fusion applications deduced by miniaturized three-point bending tests, Int. J. Refract. Met. Hard Mater. 95 (2021) http://dx.doi.org/10.1016/j.ijrmhm.2020.105464.

[8] M. Dürrschnabel, M. Klimenkov, U. Jäntsch, M. Rieth, H.C. Schneider, D. Terentyev, New insights into microstructure of neutron-irradiated tungsten, Sci. Rep. 11 (1) (2021) http://dx.doi.org/10.1038/s41598-021-86746-6.

[9] X. Hu, T. Koyanagi, M. Fukuda, Y. Katoh, L.L. Snead, B.D. Wirth, Defect evolution in single crystalline tungsten following low temperature and low dose neutron irradiation, J. Nucl. Mater. 470 (2016) 278–289, http://dx.doi.org/10.1016/j.jnucmat.2015.12.040.

[10] M. Fujitsuka, B. Tsuchiya, I. Mutoh, T. Tanabe, T. Shikama, Effect of neutron irradiation on thermal diffusivity of tungsten–rhenium alloys, J. Nucl. Mater. 283–287 (2000) 1148–1151, http://dx.doi.org/10.1016/S0022-3115(00)00170-7, URL https://linkinghub.elsevier.com/retrieve/pii/S0022311500001707.

[11] X. Zhang, Z. Gong, J. Huang, B. Yu, Texture evolution of tungsten materials during recrystallization, Mater. Res. Express 7 (2020) 56513, http://dx.doi.org/10.1088/2053-1591/ab8df4, URL https://doi.org/10.1088/2053-1591/ab8df4.

[12] S. Nogami, I. Ozawa, D. Asami, N. Matsuta, S. Nakabayashi, S. Baumgärtner, P. Lied, K. Yabuuchi, T. Miyazawa, Y. Kikuchi, M. Wirtz, M. Rieth, A. Hasegawa, Tungsten–tantalum alloys for fusion reactor applications, J. Nucl. Mater. 566 (2022) http://dx.doi.org/10.1016/j.jnucmat.2022.153740.

[13] M.R. Gilbert, L.W. Packer, T. Stainer, Experimental validation of inventory simulations on molybdenum and its isotopes for fusion applications, Nucl. Fusion 60 (10) (2020) http://dx.doi.org/10.1088/1741-4326/aba99c.

[14] L. Zhang, Y. Du, W. Han, X. Yi, P. Liu, K. Yoshida, T. Toyama, C. Xu, Q. Zhan, Y. Nagai, S. Ohnuki, F. Wan, The neglected activation of tantalum in reduced activation materials, Nucl. Mater. Energy 35 (2023) http://dx.doi.org/10.1016/j.nme.2023.101432.

[15] G. Bailey, O. Vilkhivskaya, M. Gilbert, Waste expectations of fusion steels under current waste repository criteria, Nucl. Fusion 61 (3) (2021) 036010, http://dx.doi.org/10.1088/1741-4326/abc933.

[16] A. Xu, D.E. Armstrong, C. Beck, M.P. Moody, G.D. Smith, P.A. Bagot, S.G. Roberts, Ion-irradiation induced clustering in W-Re-Ta, W-Re and W-Ta alloys: An atom probe tomography and nanoindentation study, Acta Mater. 124 (2017) 71–78, http://dx.doi.org/10.1016/j.actamat.2016.10.050, URL https://linkinghub.elsevier.com/retrieve/pii/S1359645416308175.

[17] S. Nogami, M. Wirtz, P. Lied, T. Chikada, Thermal shock behavior under deuterium plasma exposure of tungsten–tantalum alloys, Phys. Scr. 96 (11) (2021) http://dx.doi.org/10.1088/1402-4896/ac1702.

[18] G. Pintsuk, H. Kurishita, J. Linke, H. Arakawa, S. Matsuo, T. Sakamoto, S. Kobayashi, K. Nakai, Thermal shock response of fine- and ultra-fine-grained tungsten-based materials, Phys. Scr. T T145 (2011) http://dx.doi.org/10.1088/0031-8949/2011/T145/014060.

[19] H. Zhou, J. Yu, W. Han, L. Cheng, C. Chen, K. Zhu, Large plastic deformation blistering and helium retention in 5% tantalum doped tungsten under 60 keV helium ions implantation, Fusion Eng. Des. 134 (2018) 43–50, http://dx.doi.org/10.1016/j.fusengdes.2018.06.014, URL https://linkinghub.elsevier.com/retrieve/pii/S0920379618305349.

[20] E. Yildirim, P. Mummery, T. Morgan, E. Jimenez-Melero, Delayed surface degradation in W-Ta alloys at 400 °C under high-fluence 40 [ev] He plasma exposure, Fusion Eng. Des. 197 (2023) 114061, http://dx.doi.org/10.1016/j.fusengdes.2023.114061.

[21] M. Wirtz, J. Linke, G. Pintsuk, L. Singheiser, I. Uytdenhouwen, Comparison of the thermal shock performance of different tungsten grades and the influence of microstructure on the damage behaviour, in: Phys. Scr. T, T145, 2011, http://dx.doi.org/10.1088/0031-8949/2011/T145/014058.

[22] Z. Wang, Y. Yuan, K. Arshad, J. Wang, Z. Zhou, J. Tang, G.H. Lu, Effects of tantalum concentration on the microstructures and mechanical properties of tungsten-tantalum alloys, Fusion Eng. Des. 125 (2017) 496–502, http://dx.doi.org/10.1016/j.fusengdes.2017.04.082.

[23] A. Reza, H. Yu, K. Mizohata, F. Hofmann, Thermal diffusivity degradation and point defect density in self-ion implanted tungsten, Acta Mater. 193 (2020) 270–279, http://dx.doi.org/10.1016/j.actamat.2020.03.034.

[24] S.E. Ferry, C.A. Dennett, K.B. Woller, M.P. Short, Inferring radiation-induced microstructural evolution in single-crystal niobium through changes in thermal transport, J. Nucl. Mater. 523 (2019) 378–382, http://dx.doi.org/10.1016/j.jnucmat.2019.06.015.

[25] R. Qiu, Y. Chen, L. Liu, Z. Liu, N. Gao, W. Hu, H. Deng, Molecular dynamics simulation of primary radiation damage in W-Ta alloys: Effect of tantalum, J. Nucl. Mater. 556 (2021) http://dx.doi.org/10.1016/j.jnucmat.2021.153162.

[26] I. Ipatova, R.W. Harrison, D. Terentyev, S.E. Donnelly, E. Jimenez-Melero, Thermal evolution of the proton irradiated structure in tungsten-5 wt% tantalum, J. Fusion Energy 36 (2017) http://dx.doi.org/10.1007/s10894-017-0145-y.

[27] X. Yi, M.L. Jenkins, M.A. Kirk, Z. Zhou, S.G. Roberts, In-situ TEM studies of 150 keV W+ ion irradiated W and W-alloys: Damage production and microstructural evolution, Acta Mater. 112 (2016) 105–120, http://dx.doi.org/10.1016/j.actamat.2016.03.051, URL https://linkinghub.elsevier.com/retrieve/pii/S135964541630204X.

[28] SRIM, TRIM - Setup and input, in: SRIM - Stopping Range of Ions in Matter, 2008, URL www.SRIM.org.

[29] R. Stoller, M. Toloczko, G. Was, A. Certain, S. Dwaraknath, F. Garner, On the use of SRIM for computing radiation damage exposure, Nucl. Instrum. Methods Phys. Res. B 310 (2013) 75–80, http://dx.doi.org/10.1016/j.nimb.2013.05.008, URL https://linkinghub.elsevier.com/retrieve/pii/S0168583X13005053.

[30] ASTM E521-96, Standard Practice for Neutron Radiation Damage Simulation by Charged-Particle Irradiation, Tech. Rep., ASTM, 2009.

[31] D. Terentyev, P. Jenus, E. Sal, A. Zinovev, C.C. Chang, C. Garcia-Rosales, M. Kocen, S. Novak, W. Van Renterghem, Development of irradiation tolerant tungsten alloys for high temperature nuclear applications, Nucl. Fusion 62 (8) (2022) http://dx.doi.org/10.1088/1741-4326/ac75fe.

[32] G. Federici, W. Biel, M.R. Gilbert, R. Kemp, N. Taylor, R. Wenninger, European Demo Design Strategy and Consequences for Materials Related Content ITER Conceptual Design, Tech. Rep., IAEA, 2017, http://dx.doi.org/10.1088/1741-4326/57/9/092002, URL https://doi.org/10.1088/1741-4326/57/9/092002.

[33] D. Stork, P. Agostini, J.-L. Boutard, D. Buckthorpe, E. Diegele, S.L. Dudarev, C. English, G. Federici, M.R. Gilbert, S. Gonzalez, A. Ibarra, C. Linsmeier, A.L. Puma, G. Marbach, L.W. Packer, B. Raj, M. Rieth, M.Q. Tran, D.J. Ward, S.J. Zinkle, Materials R&D for a timely DEMO: Key findings and recommendations of the EU roadmap materials assessment group, Fusion Eng. Des. 89 (7–8) (2014) 1586–1594, http://dx.doi.org/10.1016/j.fusengdes.2013.11.007.

[34] O.W. Käding J', H. Skurk, A.A. Maznev, E. Matthias, Transient Thermal Gratings at Surfaces for of Bulk Materials and Thin Films, Tech. Rep., Vol. 61, 1995, pp. 253–261.

[35] F. Hofmann, D.R. Mason, J.K. Eliason, A.A. Maznev, K.A. Nelson, S.L. Dudarev, Non-contact measurement of thermal diffusivity in ion-implanted nuclear materials, Nat. Publ. Group (2015) http://dx.doi.org/10.1038/srep16042, URL www.nature.com/scientificreports/.

[36] F. Hofmann, M. Short, C. Dennett, Transient grating spectroscopy: An ultrarapid, nondestructive materials evaluation technique, MRS Bull. 44 (5) (2019) http://dx.doi.org/10.1557/mrs.2019.104, URL www.mrs.org/bulletin.

[37] C.A. Dennett, M.P. Short, Time-resolved, dual heterodyne phase collection transient grating spectroscopy, Appl. Phys. Lett. 110 (21) (2017) http://dx.doi.org/10.1063/1.4983716.

[38] A.P. Wylie, K.B. Woller, S.A. Al Dajani, B.R. Dacus, E.J. Pickering, M. Preuss, M.P. Short, Thermal diffusivity in ion-irradiated single-crystal iron, chromium, vanadium, and tungsten measured using transient grating spectroscopy, J. Appl. Phys. 132 (4) (2022) http://dx.doi.org/10.1063/5.0089048.

[39] D.B. Williams, C.B. Carter, Transmission Electron Microscopy: Diffraction, Imaging and Spectroscopy, second ed., Springer, 2016.

[40] Y. Chen, J. Fang, L. Liu, W. Hu, N. Gao, F. Gao, H. Deng, Development of the interatomic potentials for W-Ta system, Comput. Mater. Sci. 163 (2019) 91–99, http://dx.doi.org/10.1016/j.commatsci.2019.03.021.

[41] A. Stukowski, Visualization and analysis of atomistic simulation data with OVITO–the open visualization tool, Modelling Simul. Mater. Sci. Eng. 18 (1) (2010) 015012, http://dx.doi.org/10.1088/0965-0393/18/1/015012, URL https://iopscience.iop.org/article/10.1088/0965-0393/18/1/015012 https://iopscience.iop.org/article/10.1088/0965-0393/18/1/015012/meta.

[42] M. Fukuda, A. Hasegawa, S. Nogami, Thermal properties of pure tungsten and its alloys for fusion applications, Fusion Eng. Des. 132 (2018) 1–6, http://dx.doi.org/10.1016/j.fusengdes.2018.04.117, URL https://linkinghub.elsevier.com/retrieve/pii/S0920379618304113.

[43] S. Cui, R.P. Doerner, M.J. Simmonds, C. Xu, Y. Wang, E. Dechaumphai, E. Fu, G.R. Tynan, R. Chen, Thermal conductivity degradation and recovery in ion beam damaged tungsten at different temperature, J. Nucl. Mater. 511 (2018) 141–147, http://dx.doi.org/10.1016/j.jnucmat.2018.09.002, URL https://linkinghub.elsevier.com/retrieve/pii/S002231151830494X.

[44] I.V. Savchenko, S.V. Stankus, Thermal Conductivity and Thermal Diffusivity of Tantalum in the Temperature Range from 293 to 1800 K *, Tech. Rep., Vol. 15, (4) 2008.

[45] A. Reza, G. He, C.A. Dennett, H. Yu, K. Mizohata, F. Hofmann, Thermal diffusivity recovery and defect annealing kinetics of self-ion implanted tungsten probed by insitu transient grating spectroscopy, Acta Mater. 232 (2022) http://dx.doi.org/10.1016/j.actamat.2022.117926.

[46] J. Habainy, Y. Dai, Y. Lee, S. Iyengar, Thermal diffusivity of tungsten irradiated with protons up to 5.8 dpa, J. Nucl. Mater. 509 (2018) 152–157, http://dx.doi.org/10.1016/j.jnucmat.2018.06.041, URL https://linkinghub.elsevier.com/retrieve/pii/S0022311518305828.

[47] F. Ferroni, X. Yi, K. Arakawa, S.P. Fitzgerald, P.D. Edmondson, S.G. Roberts, High temperature annealing of ion irradiated tungsten, Acta Mater. 90 (2015) 380–393, http://dx.doi.org/10.1016/j.actamat.2015.01.067, URL https://linkinghub.elsevier.com/retrieve/pii/S1359645415000804.

[48] D. Papadakis, K. Mergia, The effect of microstructure on recovery and recrystallization after annealing of two neutron irradiated ITER specification tungsten, Int. J. Refract. Met. Hard Mater. 121 (2024) 106657, http://dx.doi.org/10.1016/j.ijrmhm.2024.106657.

[49] T.E. Ray, J.K. Tripathi, A. Hassanein, Synergistic effects of W–Ta alloys exposed to various ELM-like fusion events, Nucl. Fusion 64 (4) (2024) 046001, http://dx.doi.org/10.1088/1741-4326/ad249c.

[50] S. Gonderman, J. Tripathi, T. Novakowski, T. Sizyuk, A. Hassanein, The effect of low energy helium ion irradiation on tungsten-tantalum (W-Ta) alloys under fusion relevant conditions, J. Nucl. Mater. 491 (2017) 199–205, http://dx.doi.org/10.1016/j.jnucmat.2017.05.009, URL https://linkinghub.elsevier.com/retrieve/pii/S0022311516312533.

[51] H. Li, C. Draxl, S. Wurster, R. Pippan, L. Romaner, Impact of d -band filling on the dislocation properties of bcc transition metals: The case of tantalum-tungsten alloys investigated by density-functional theory, Phys. Rev. B 95 (9) (2017) http://dx.doi.org/10.1103/PhysRevB.95.094114.

[52] M. Jin, P. Cao, M.P. Short, Thermodynamic mixing energy and heterogeneous diffusion uncover the mechanisms of radiation damage reduction in single-phase Ni-Fe alloys, Acta Mater. 147 (2018) 16–23, http://dx.doi.org/10.1016/j.actamat.2017.12.064.

[53] X.S. Kong, X. Wu, Y.W. You, C.S. Liu, Q.F. Fang, J.L. Chen, G.N. Luo, Z. Wang, First-principles calculations of transition metal-solute interactions with point defects in tungsten, Acta Mater. 66 (2014) 172–183, http://dx.doi.org/10.1016/j.actamat.2013.11.044.

[54] Z. Wang, L. Gao, X.-L. Zhu, Y. Yuan, S. Wang, L. Cheng, G.-H. Lu, Effect of rhenium on defects evolution behavior in tungsten under irradiation, Nucl. Fusion 61 (3) (2021) 036037, http://dx.doi.org/10.1088/1741-4326/abd920.